Coupled EFGM and FFEM for unbounded problems

IOP Conf. Series: Materials Science and Engineering **10** (2010) 012225 doi:10.1088/1757-899X/10/1/012225

Coupled EFGM and FFEM for Unbounded Problems

K N Rajesh and B. N. Rao[1]
Structural Engineering Division, Department of Civil Engineering, Indian Institute of Technology Madras, Chennai, INDIA

E-mail: bnrao@iitm.ac.in

Abstract. This paper presents a coupling technique for integrating the element-free Galerkin method (EFGM) with the fractal finite element method (FFEM) to analyze unbounded problems in the half-space. FFEM is adopted to model the far field of an unbounded domain and EFGM is used in the near field. In the transition region interface elements are employed. The proposed method combines the best features of EFGM and FFEM, in the sense that no structured mesh or special enriched basis functions are necessary. The numerical results show that the proposed method performs extremely well converging rapidly to the analytical solution.

1. Introduction

Meshless or meshfree approaches have gained significant popularity in recent years. Among all meshfree methods, the EFGM [1, 2] is particularly appealing, due to its simplicity and a formulation that corresponds to the well-established finite element method (FEM). A major advantage of these approaches is that an unstructured distribution of nodes can be used, and adaptive procedures introducing more nodes in regions of high error can be implemented easily.

Often in engineering practice, one is faced with problems where the media bounding the structure is much larger than the domain of interest, such as those that arise in soil-structure and fluid-structure interactions. In all these cases, the surrounding media can be treated as infinite and these are collectively called unbounded domain problems. As in the FEM, solution of such unbounded problems can only be achieved using meshfree methods through truncation of the domain of interest at some distance 'sufficiently far' from the region of interest.

Recently methods based on fractal geometry concepts to generate infinite number of finite elements around the crack tip to capture the crack tip singularity have been developed or investigated to solve linear elastic fracture mechanics (LEFM) problems [3], and unbounded problems in the half-space [4]. Basically, in a semi-infinite problem FFEM separates the half-space into a regular and an unbounded fractal finite element (FFE) domain (as shown in Figure 1). Both the regular and the unbounded regions are modelled by conventional, isoparametric finite elements. However, within the unbounded region an infinite number of elements are generated by a self-similar, fractal process to model the far field of an unbounded domain. The global interpolating functions in the form of a truncated infinite series are employed to transform the infinite number of nodal displacements to a small number of unknown coefficients associated with the global interpolating functions. Due to geometrical similarity,

[1] To whom any correspondence should be addressed.

transformation for one layer is enough as the relevant entries of the transformed matrix after assembling all layers are infinite geometric series of the similarity ratio that can be summed analytically to be assembled to the global stiffness matrix. The contributions of the infinite number of elements in the unbounded region are therefore fully accounted for while the number of degrees of freedom involved remains finite.

This paper presents a coupling technique for integrating EFGM with FFEM to analyze unbounded problems in the half-space.

2. Fractal Finite Element Method

As depicted in the Figure 1, consider a semi-infinite problem, in which the half-space is divided into the regular FE domain R_1 and the unbounded FFE domain R_2 by the boundary Γ_0. In the regular FE region, conventional finite elements are used and the nodal displacements are the unknowns. In the FFE region extending to infinity, the FFE technique is adopted. Taking the origin as the centre of similarity and using $\alpha(>1)$ as the similarity ratio (or proportional constant), an infinite set of curves $\{\Gamma_1,\Gamma_2,\ldots\}$, similar to Γ_0 but with ratios $\alpha^1,\alpha^2,\alpha^3,\ldots$ is generated in the unbounded domain. Between the two curves Γ_{k-1} and Γ_k, the region is named the *k*-th layer. A set of straight lines that emanate from the origin and pass through the corner nodes on Γ_0 is then created, dividing the unbounded region into a fractal mesh of similar elements. All nodes on Γ_0 are called the master nodes (*m*) while those beyond are called the slave nodes (*s*).

2.1. Global Interpolation Functions for Torsionless Axisymmetry

Many problems of solids of revolution deformed by loads symmetrical about the axis of symmetry have the displacement components u, and w given below as their solutions [4]:

$$u=\sum_{n=0}^{\infty}\frac{R^{-n-3}}{2G}A_nG_{11}(n,\psi)+\sum_{n=0}^{\infty}\frac{R^{-n-1}}{2G}B_nG_{12}(n,\psi), \tag{1}$$

$$w=\sum_{n=0}^{\infty}\frac{R^{-n-3}}{2G}A_nG_{21}(n,\psi)+\sum_{n=0}^{\infty}\frac{R^{-n-1}}{2G}B_nG_{22}(n,\psi), \tag{2}$$

where $G_{ij}(n,\psi)$ with $i,j=1,2,$ are the angular functions. For FFE, truncations of these expressions will be used as the interpolating functions.

2.2. Fractal Transformation

In the regular region in Figure 1, R_1, for linear continuum axisymmetric elements according to the conservation of strain energy the stiffness equation system can be written as

$$\boldsymbol{K}\boldsymbol{d}=\boldsymbol{f}\ . \tag{3}$$

The stiffness matrix $\boldsymbol{K}$ is determined as follows:

$$\boldsymbol{K}=\int_{-1}^{1}\int_{-1}^{1}\boldsymbol{B}^T\boldsymbol{D}\boldsymbol{B}(2\pi r)\det\boldsymbol{J}d\xi d\eta\,. \tag{4}$$

The stiffness matrix equation for the regular FEM domain can be assembled and then partitioned with respect to the nodes other than the master nodes (*r*) and the master nodes (*m*) as follows,

$$\begin{bmatrix}\boldsymbol{K}_{rr}^R & \boldsymbol{K}_{rm}^R\\ \boldsymbol{K}_{mr}^R & \boldsymbol{K}_{mm}^R\end{bmatrix}\begin{Bmatrix}\boldsymbol{d}_r\\ \boldsymbol{d}_m\end{Bmatrix}=\begin{Bmatrix}\boldsymbol{f}_r^R\\ \boldsymbol{f}_m^R\end{Bmatrix}, \tag{5}$$

where $\boldsymbol{d}_r$ are the displacements of the nodes in the regular region other than the master nodes (*r*), and $\boldsymbol{d}_m$ are the displacements of the master nodes (*m*), etc.

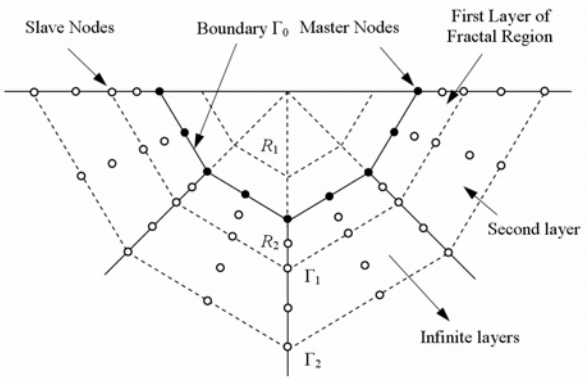

Figure 1. Fractal finite mesh for unbounded domain

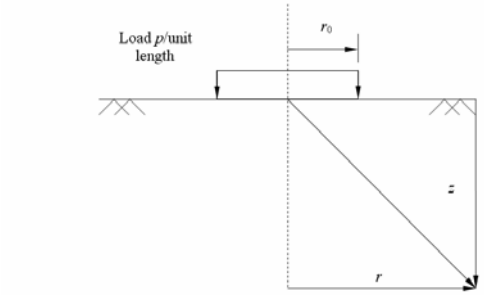

Figure 3. Uniform vertical ring load acting on surface of semi–infinite mass

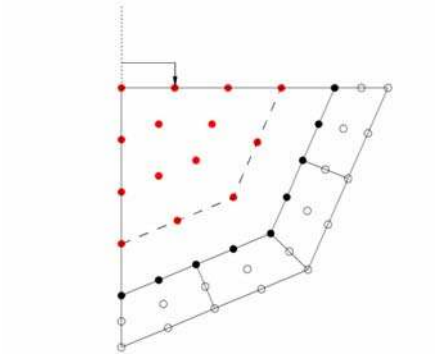

Figure 4. Coupled EFGM–FFEM discretization of semi–infinite mass with uniform vertical ring load acting on surface

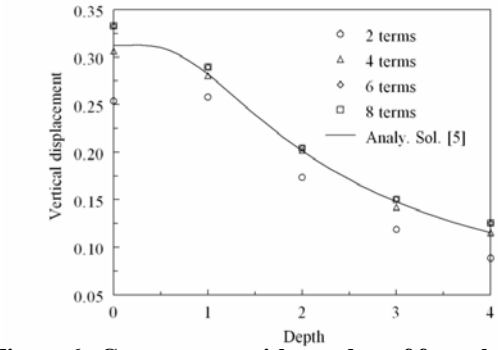

Figure 6. Convergence with number of fractal transformation terms (Example 1)

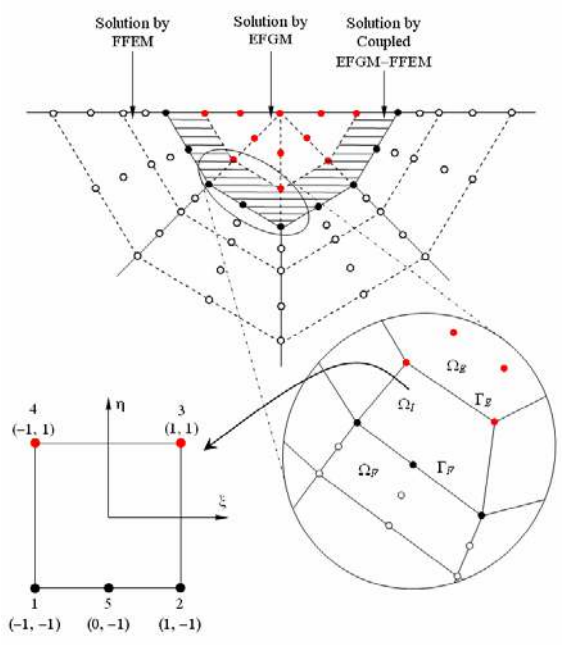

Figure 2. Details of EFGM–FFEM coupling

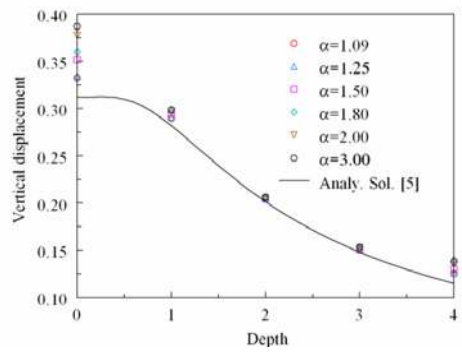

Figure 5. Convergence with similarity ratio (Example 1)

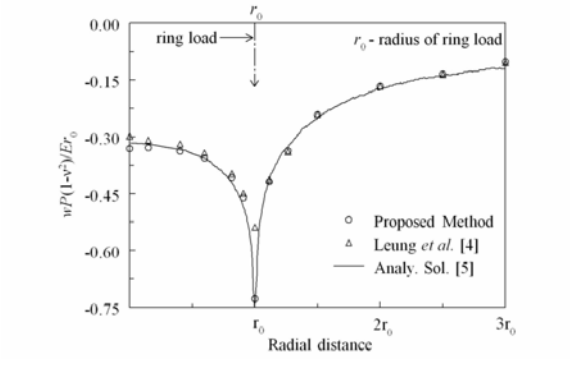

Figure 7. Comparison of radial variation of vertical displacement at $z = 0$ (Example 1)

In the unbounded region R_2, each layer is created from the adjacent inner layer using the same similarity ratio throughout. The infinite number of nodal displacements will be transformed into a finite set of generalized coordinates using the global interpolation functions given in Equations 1 and 2. For the first layer in the unbounded region, the stiffness equation system

$$\boldsymbol{K}^{1st}\boldsymbol{d}^{1st} = \boldsymbol{f}^{1st}, \tag{6}$$

can be partitioned with respect to the master nodes (*m*) and the slave nodes (*s*) as follows,

$$\begin{bmatrix} \boldsymbol{K}_{mm}^{1st} & \boldsymbol{K}_{ms}^{1st} \\ \boldsymbol{K}_{sm}^{1st} & \boldsymbol{K}_{ss}^{1st} \end{bmatrix} \begin{Bmatrix} \boldsymbol{d}_m \\ \boldsymbol{d}_s^{1st} \end{Bmatrix} = \begin{Bmatrix} \boldsymbol{f}_m^{1st} \\ \boldsymbol{f}_s^{1st} \end{Bmatrix}, \tag{7}$$

where $\boldsymbol{d}_s^{1st}$ are the displacements of the slave nodes (*s*) in the first layer of the unbounded region. Using the global interpolation functions given in Equations 1 and 2, $\boldsymbol{d}_s^{1st}$ can be expressed as a function of the generalized coordinates $\boldsymbol{a} = \{A_0, B_0, A_1, B_1, \ldots\}^T$ as

$$\boldsymbol{d}_s^{1st}(R,\psi) = \boldsymbol{T}_s^{1st}(R,\psi)\boldsymbol{a}, \tag{8}$$

where $\boldsymbol{T}_s^{1st} = \boldsymbol{T}_s^{1st}(R,\psi)$ is a transformation matrix in terms of the polar coordinates (R,ψ) for the slave nodes (*s*) in the first layer, evaluated from Equations 1 and 2.

Using the transformation matrix $\boldsymbol{T}_s^{1st}(R,\psi)$ Equation 7 can be transformed into

$$\begin{bmatrix} \boldsymbol{K}_{mm}^{1st} & \boldsymbol{K}_{ms}^{1st}\boldsymbol{T}_s^{1st} \\ \left(\boldsymbol{T}_s^{1st}\right)^T \boldsymbol{K}_{sm}^{1st} & \left(\boldsymbol{T}_s^{1st}\right)^T \boldsymbol{K}_{ss}^{1st}\boldsymbol{T}_s^{1st} \end{bmatrix} \begin{Bmatrix} \boldsymbol{d}_m \\ \boldsymbol{a} \end{Bmatrix} = \begin{Bmatrix} \boldsymbol{f}_m^{1st} \\ \left(\boldsymbol{T}_s^{1st}\right)^T \boldsymbol{f}_s^{1st} \end{Bmatrix}. \tag{9}$$

Since the second and subsequent layers in the unbounded region i.e. $k \geq 2$, comprises of only the slave nodes (*s*), the stiffness equation system can be written as follows

$$\boldsymbol{K}_s^{kth}\boldsymbol{d}_s^{kth} = \boldsymbol{f}_s^{kth}, \tag{10}$$

or, using the transformation matrix $\boldsymbol{T}_s^{1st}(R,\psi)$ Equation 10 can be expressed in terms of the generalized coordinates $\boldsymbol{a}$ as follows,

$$\left(\boldsymbol{T}_s^{kth}\right)^T \boldsymbol{K}_s^{kth}\boldsymbol{T}_s^{kth}\boldsymbol{a} = \left(\boldsymbol{T}_s^{kth}\right)^T \boldsymbol{f}_s^{kth}. \tag{11}$$

The final assembled global stiffness equation system has the form

$$\begin{bmatrix} \boldsymbol{K}_{rr}^{R} & \boldsymbol{K}_{rm}^{R} & \boldsymbol{0} \\ \boldsymbol{K}_{mr}^{R} & \boldsymbol{K}_{mm}^{R} + \boldsymbol{K}_{mm}^{1st} & \bar{\boldsymbol{K}}_{ms}^{1st} \\ \boldsymbol{0} & \bar{\boldsymbol{K}}_{sm}^{1st} & \bar{\boldsymbol{K}}_{ss}^{1st} + \bar{\boldsymbol{K}}_{s}^{inn} \end{bmatrix} \begin{Bmatrix} \boldsymbol{d}_r \\ \boldsymbol{d}_m \\ \boldsymbol{a} \end{Bmatrix} = \begin{Bmatrix} \boldsymbol{f}_r^{R} \\ \boldsymbol{f}_m^{R} + \boldsymbol{f}_m^{1st} \\ \bar{\boldsymbol{f}}_s^{1st} + \bar{\boldsymbol{f}}_s^{inn} \end{Bmatrix}, \tag{12}$$

where $\bar{\boldsymbol{K}}_{ms}^{1st} = \boldsymbol{K}_{ms}^{1st}\boldsymbol{T}_s^{1st}$, $\bar{\boldsymbol{K}}_{ss}^{1st} = \left(\boldsymbol{T}_s^{1st}\right)^T \boldsymbol{K}_{ss}^{1st}\boldsymbol{T}_s^{1st}$ and $\bar{\boldsymbol{f}}_s^{1st} = \left(\boldsymbol{T}_s^{1st}\right)^T \boldsymbol{f}_s^{1st}$, etc.

Consider two elements, denoted by 1 and 2, which are similar in the r and z directions with α being the proportional constant, then

$$\det \boldsymbol{J}_2 = \alpha^2 \det \boldsymbol{J}_1 \quad \text{and} \quad \boldsymbol{B}_2 = \frac{1}{\alpha}\boldsymbol{B}_1 \quad \text{since} \quad r_2 = \alpha r_1. \tag{13}$$

Therefore, for a continuum axisymmetric element,

$$\boldsymbol{K}_2 = \int_{-1}^{1}\int_{-1}^{1} \boldsymbol{B}_2{}^T \boldsymbol{D}\boldsymbol{B}_2 (2\pi r_2) \det \boldsymbol{J}_2 d\xi d\eta = \alpha \boldsymbol{K}_1. \tag{14}$$

It follows that

$$\boldsymbol{K}_k = \alpha^{k-1}\boldsymbol{K}_1 \quad \text{and} \quad \boldsymbol{T}_k = \boldsymbol{T}_1 \text{Diag}[\alpha_i] = \boldsymbol{T}_1 \text{Diag}\left[\alpha^{-(k-1)n_i}\right], \tag{15}$$

where

$$\alpha_i = \alpha^{-(k-1)n_i}, \tag{16}$$

is a scaling function and

$$n_i = \begin{cases} (i+5)/2 & \text{for } i = 1,3,\ldots \\ i/2 & \text{for } i = 2,4,\ldots \end{cases} \tag{17}$$

Therefore,

$$\sum_{k=2}^{\infty} \boldsymbol{T}_k^T \boldsymbol{K}_k \boldsymbol{T}_k = \sum_{k=2}^{\infty} \mathrm{Diag}\left[\alpha_i\right]^T \boldsymbol{T}_1^T \alpha^{(k-1)} \boldsymbol{K}_1 \boldsymbol{T}_1 \mathrm{Diag}\left[\alpha_j\right] = \left[\bar{\alpha}_{ij} \bar{\boldsymbol{k}}_{ij}\right], \tag{18}$$

where

$$\bar{\alpha}_{ij} = \sum_{k=2}^{\infty} \alpha^{-(k-1)n_i} \alpha^{(k-1)} \alpha^{-(k-1)n_j} = \left[\alpha^{(n_i+n_j-1)} - 1\right]^{-1} \quad \text{and} \quad \bar{\boldsymbol{k}}_{ij} = \boldsymbol{T}_1^T \boldsymbol{K}_1 \boldsymbol{T}_1 \ . \tag{19}$$

A similar procedure can be applied to the global generalized force.

3. Coupling Procedure

Due to the close relation between plane and axisymmetric analyses, axis labels x_1 - x_2, instead of r - z, are adopted in sections 3 and 4. The coupling between FFEM and EFGM domains is accomplished by introducing interface elements in between those domains (see Figure 2). In these interface elements, a hybrid displacement approximation is defined that satisfies displacement continuity across the interface boundaries. For displacement approximation in the Galerkin procedure, both FE and EFG use similar forms:

$$u_i^h(\boldsymbol{x}) = \sum_{I=1}^{n} \tilde{\Phi}_I(\boldsymbol{x}) d_{iI} \ . \tag{20}$$

3.1. FE shape functions

The displacement approximation u_i, in an isoparametric element is given by

$$u_i^h(\boldsymbol{x}) = \sum_{I=1}^{n_{en}} N_I\left(\xi(\boldsymbol{x})\right) d_{iI}, \quad \boldsymbol{x} \in \Omega_F^e \ , \tag{21}$$

where n_{en} is the number of element nodes. Because Q8 (8-node serendipity) and L9 (9-node Lagrangian) elements are used in FFEM discretization, in the present study 5-node element is adopted for interface elements.

3.2. EFG shape functions

In the EFG method, the displacement is approximated by moving least-squares approximations (MLS) [1, 2]. The MLS approximation $u_i^h(\boldsymbol{x})$ is given by

$$u_i^h(\boldsymbol{x}) = \sum_{I=1}^{n_{sn}} \Phi_I(\boldsymbol{x}) d_{iI} = \boldsymbol{\Phi}^T(\boldsymbol{x}) \boldsymbol{d}_i, \quad \boldsymbol{x} \in \Omega_E \ , \tag{22}$$

where the EFG shape functions are defined as

$$\Phi_I(\boldsymbol{x}) = \sum_{J=1}^{m_b} p_J(\boldsymbol{x}) \left[\boldsymbol{A}^{-1}(\boldsymbol{x}) \boldsymbol{C}(\boldsymbol{x})\right]_{JI} \ . \tag{23}$$

3.3. Interface displacement approximation

A detailed schematic of interface domain is shown in Figure 2. In Ω_E, the displacement at a point is approximated using the MLS approximants in Equation 22, and in Ω_F, the FE interpolants in Equation 21 are employed in each element subdomain Ω_F^e. In Ω_I, the interface region, the displacement at a point is approximated using the following expression:

$$\begin{aligned} u_i^h(\boldsymbol{x}) &= u_i^{FE}(\boldsymbol{x}) + R(\boldsymbol{x})\left[u_i^{EFG}(\boldsymbol{x}) - u_i^{FE}(\boldsymbol{x})\right] \\ &\equiv [1-R(\boldsymbol{x})]u_i^{FE}(\boldsymbol{x}) + R(\boldsymbol{x})u_i^{EFG}(\boldsymbol{x}) \qquad \boldsymbol{x}\in\Omega_I \end{aligned}, \tag{24}$$

where u_i^{FE} and u_i^{EFG} are approximations for u_i, in Ω_I given by the FE and EFG approximations, respectively, and $R(\boldsymbol{x})$ is a ramp function for coupling the FE and EFG regions. $R(\boldsymbol{x})$ is defined using the FE shape functions as:

$$R(\boldsymbol{x}) = \sum_{\substack{J \\ x_I\in\Gamma_E}} N_J(\boldsymbol{x}). \tag{25}$$

The interface shape functions can be developed by substituting the displacement approximations Equations 21 and 22 into Equation 24:

$$\begin{aligned} u_i^h(\boldsymbol{x}) &= [1-R(\boldsymbol{x})]\sum_{I=1}^{n_{en}} N_I\left(\xi(\boldsymbol{x})\right)d_{iI} + R(\boldsymbol{x})\sum_{I=1}^{n_{sn}}\Phi_I(\boldsymbol{x})d_{iI} \\ &\equiv \sum_{I=1}^{n_{sn}}\bar{\Phi}_I(\boldsymbol{x})d_{iI} \qquad \boldsymbol{x}\in\Omega_I^e \end{aligned}, \tag{26}$$

where the interface shape functions $\bar{\Phi}_I(\boldsymbol{x})$ are

$$\bar{\Phi}_I(\boldsymbol{x}) = \begin{cases} \left[1-R(\boldsymbol{x})\right]N_I\left(\xi(\boldsymbol{x})\right) + R(\boldsymbol{x})\Phi_I(\boldsymbol{x}) & \boldsymbol{x}_I\in\Omega_I^e \\ R(\boldsymbol{x})\Phi_I(\boldsymbol{x}) & \boldsymbol{x}_I\notin\Omega_I^e \end{cases}. \tag{27}$$

4. Variational formulation and discretization

For small displacements in axisymmetric, homogeneous, isotropic, and linear-elastic solids, the equilibrium equations and boundary conditions are

$$\nabla\cdot\boldsymbol{\sigma} + \boldsymbol{b} = \boldsymbol{0} \ \text{ in } \Omega, \tag{28}$$

and

$$\begin{aligned} &\boldsymbol{\sigma}\cdot\boldsymbol{n} = \bar{\boldsymbol{t}} \quad \text{on} \quad \Gamma_t \ \text{(natural boundary conditions)} \\ &\boldsymbol{u} = \bar{\boldsymbol{u}} \quad \text{on} \quad \Gamma_u \ \text{(essential boundary conditions)} \end{aligned}, \tag{29}$$

respectively.

Since the nodal parameters and the nodal displacements are same in the finite elements, essential boundary conditions in the FFEM region can be applied by adopting the procedures similar to that in the FE analysis. In the following the concept of application of essential boundary conditions in the EFGM and the transition regions is outlined. For an easy illustration, consider a single boundary constraint, $\bar{u}_i(\boldsymbol{x}_J) = g_i(\boldsymbol{x}_J)$ applied at node J (which belongs to the EFGM region or the transition region) in the direction of x_i coordinate. Then, the variational form given by Equations 28 and 29 can be expressed by

$$\int_\Omega \boldsymbol{\sigma}^T\delta\boldsymbol{\epsilon}d\Omega \ + f_i(\boldsymbol{x}_J)\delta u_i(\boldsymbol{x}_J) = \int_\Omega \boldsymbol{b}^T\delta\boldsymbol{u}d\Omega \ - \int_{\Gamma_t}\bar{\boldsymbol{t}}^T\delta\boldsymbol{u}d\Gamma \ , \tag{30}$$

$$\delta f_i(\boldsymbol{x}_J)\left[u_i(\boldsymbol{x}_J) - g_i(\boldsymbol{x}_J)\right] = 0, \tag{31}$$

where $f_i(\boldsymbol{x}_J)$ and $u_i(\boldsymbol{x}_J)$ are the *i*-th component of $\boldsymbol{f}(\boldsymbol{x}_J)$ and $\boldsymbol{u}(\boldsymbol{x}_J)$, respectively. From Equations 21 and 22 the approximation of $u_i(\boldsymbol{x}_J)$ can be written as

$$u_i^h(\boldsymbol{x}_J) = \sum_{I=1}^{N}\tilde{\Phi}_I(\boldsymbol{x}_J)d_{iI} = \tilde{\boldsymbol{\Phi}}_J^{i\,T}\boldsymbol{d}, \tag{32}$$

where

$$\tilde{\boldsymbol{\Phi}}_J^{i\,T} = \begin{cases} \left\{\tilde{\Phi}_1(\boldsymbol{x}_J), 0, \tilde{\Phi}_2(\boldsymbol{x}_J), 0, \cdots, \tilde{\Phi}_N(\boldsymbol{x}_J), 0\right\} & \text{when } i = 1 \\ \left\{0, \tilde{\Phi}_1(\boldsymbol{x}_J), 0, \tilde{\Phi}_2(\boldsymbol{x}_J), \cdots, 0, \tilde{\Phi}_N(\boldsymbol{x}_J)\right\} & \text{when } i = 2 \end{cases}, \tag{33}$$

with

$$\tilde{\Phi}_I(\boldsymbol{x}) = \begin{cases} N_I(\xi(\boldsymbol{x})) & \boldsymbol{x} \in \Omega_F^e \\ \Phi_I(\boldsymbol{x}) & \boldsymbol{x} \in \Omega_E \\ \bar{\Phi}_I(\boldsymbol{x}) & \boldsymbol{x} \in \Omega_I^e \end{cases}, \tag{34}$$

and

$$\boldsymbol{d} = \{d_{11} \quad d_{21} \quad d_{12} \quad d_{22} \quad \cdots \quad d_{1N} \quad d_{2N}\}^T. \tag{35}$$

Using Equations 32-35 into the coupled EFGM-FFEM discretization (involving the master nodes (*m*), the slave nodes (*s*) and the nodes other than the master nodes (*r*)) of Equations 30 and 31 and application of the FFEM concepts outlined in section 2 results in

$$\begin{bmatrix} \begin{Bmatrix} \boldsymbol{K}_{rr}^R & \boldsymbol{K}_{rm}^R & \boldsymbol{0} \\ \boldsymbol{K}_{mr}^R & \boldsymbol{K}_{mm}^R + \boldsymbol{K}_{mm}^{1st} & \boldsymbol{K}_{ms}^{1st}\boldsymbol{T}_s^{1st} \\ \boldsymbol{0} & \left(\boldsymbol{T}_s^{1st}\right)^T \boldsymbol{K}_{sm}^{1st} & \left(\boldsymbol{T}_s^{1st}\right)^T \boldsymbol{K}_{ss}^{1st}\boldsymbol{T}_s^{1st} + \bar{\alpha}_{ij}\left(\boldsymbol{T}_s^{1st}\right)^T \boldsymbol{K}^{1st}\left(\boldsymbol{T}_s^{1st}\right) \end{Bmatrix} & \tilde{\boldsymbol{\Phi}}_J^{\,i} \\ \tilde{\boldsymbol{\Phi}}_J^{\,iT} & 0 \end{bmatrix} \begin{Bmatrix} \begin{Bmatrix} \boldsymbol{d}_r \\ \boldsymbol{d}_m \\ \boldsymbol{a} \end{Bmatrix} \\ f_i(\boldsymbol{x}_J) \end{Bmatrix}, \tag{36}$$

$$= \begin{Bmatrix} \begin{Bmatrix} \boldsymbol{f}_r^R \\ \boldsymbol{f}_m^R + \boldsymbol{f}_m^{1st} \\ \left(\boldsymbol{T}_s^{1st}\right)^T \boldsymbol{f}_s^{1st} + \bar{\alpha}_i\left(\boldsymbol{T}_s^{1st}\right)^T \boldsymbol{f}^{1st} \end{Bmatrix} \\ g_i(\boldsymbol{x}_J) \end{Bmatrix}$$

where the matrices $\boldsymbol{K}_{rr}^R$, $\boldsymbol{K}_{rm}^R$, $\boldsymbol{K}_{mm}^R$, $\boldsymbol{K}_{mm}^{1st}$, $\boldsymbol{K}_{ms}^{1st}$, $\boldsymbol{K}_{ss}^{1st}$ are obtained by partitioning and transforming the global stiffness matrix whose IJ –th component is given by,

$$[\boldsymbol{K}]_{IJ} = \int_\Omega \boldsymbol{B}_I^T \boldsymbol{D}\boldsymbol{B}_J d\Omega \in \mathsf{L}\left(\Re^2 \times \Re^2\right), \tag{37}$$

and the vectors $\boldsymbol{f}_r^R$, $\boldsymbol{f}_m^R$, $\boldsymbol{f}_m^{1st}$, $\boldsymbol{f}_s^{1st}$ are obtained by partitioning and transforming the global force vector whose I -th component is given by,

$$[\boldsymbol{f}]_I = \int_\Omega \tilde{\Phi}_I \boldsymbol{b}^T d\Omega - \int_{\Gamma_t} \tilde{\Phi}_I \bar{\boldsymbol{t}}^T d\Gamma \in \Re^2. \tag{38}$$

In the present study, standard Gaussian quadrature is used to evaluate the integrals for assembling the stiffness matrix and the force vector by adopting 8×8 quadrature in the EFGM and in the transition regions. In the FFEM region 2×2 quadrature is used.

5. Essential boundary conditions

Lack of Kronecker delta properties in the meshless shape functions, Φ_I poses some difficulties in imposing essential boundary conditions in the EFGM and in the transition regions. In this work, a full transformation method [2] is adopted.

Consider the following transformation relating the nodal parameters and the nodal displacements of the master nodes (*m*), and the nodes other than the master nodes (*r*),

$$\begin{Bmatrix} \hat{\boldsymbol{d}}_r \\ \hat{\boldsymbol{d}}_m \end{Bmatrix} = \boldsymbol{\Lambda} \begin{Bmatrix} \boldsymbol{d}_r \\ \boldsymbol{d}_m \end{Bmatrix}, \tag{39}$$

where $\hat{\boldsymbol{d}}_m$ and $\hat{\boldsymbol{d}}_r$ are respectively the nodal displacements of the master nodes (*m*), and the nodes other than the master nodes (*r*), and

$$\boldsymbol{\Lambda} = \begin{bmatrix} \overbrace{\begin{Bmatrix} \tilde{\boldsymbol{\Phi}}_1^{1T} \\ \tilde{\boldsymbol{\Phi}}_1^{2T} \\ \tilde{\boldsymbol{\Phi}}_2^{1T} \\ \tilde{\boldsymbol{\Phi}}_2^{2T} \\ \vdots \end{Bmatrix}}^{\text{nodes other than master nodes in regular region } (r)} & \boldsymbol{0} \\ \boldsymbol{0} & \underbrace{\begin{Bmatrix} 1 & 0 & 0 & 0 & 0 \\ 0 & 1 & 0 & 0 & 0 \\ \vdots & \vdots & \ddots & \vdots & \vdots \\ 0 & 0 & 0 & 1 & 0 \\ 0 & 0 & 0 & 0 & 1 \end{Bmatrix}}_{\text{master nodes } (m)} \end{bmatrix} \in \mathsf{L}\left(\Re^{2(r+m)} \times \Re^{2(r+m)}\right), \tag{40}$$

is the transformation matrix. Multiplying the first two sets of matrix equations in Equation 36 by $\boldsymbol{\Lambda}^{-T}$, one obtains

$$\begin{bmatrix} \begin{Bmatrix} \boldsymbol{\Lambda}^{-T} \begin{Bmatrix} \boldsymbol{K}_{rr} & \boldsymbol{K}_{rm} \\ \boldsymbol{K}_{mr} & \boldsymbol{K}_{mm} + \boldsymbol{K}_{mm}^{1st} \end{Bmatrix} & \begin{Bmatrix} \boldsymbol{0} \\ \bar{\boldsymbol{K}}_{ms}^{1st} \end{Bmatrix} \\ \begin{Bmatrix} \boldsymbol{0} & \bar{\boldsymbol{K}}_{sm}^{1st} \end{Bmatrix} & \begin{Bmatrix} \bar{\boldsymbol{K}}_{ss}^{1st} + \bar{\boldsymbol{K}}_{s}^{inn} \end{Bmatrix} \end{Bmatrix} & \begin{Bmatrix} \boldsymbol{\Lambda}^{-T} \begin{Bmatrix} \tilde{\boldsymbol{\Phi}}_J^{\,i} \\ \boldsymbol{0} \end{Bmatrix} \\ \boldsymbol{0} \end{Bmatrix} \\ \begin{Bmatrix} \tilde{\boldsymbol{\Phi}}_J^{\,iT} & \boldsymbol{0} \end{Bmatrix} \quad \boldsymbol{0} & 0 \end{bmatrix} \begin{Bmatrix} \begin{Bmatrix} \boldsymbol{d}_r \\ \boldsymbol{d}_m \end{Bmatrix} \\ \boldsymbol{a} \\ f_i(\boldsymbol{x}_J) \end{Bmatrix} = \begin{Bmatrix} \begin{Bmatrix} \boldsymbol{\Lambda}^{-T} \begin{Bmatrix} \boldsymbol{f}_r \\ \boldsymbol{f}_m + \boldsymbol{f}_m^{1st} \end{Bmatrix} \\ \bar{\boldsymbol{f}}_s^{1st} + \bar{\boldsymbol{f}}_s^{inn} \end{Bmatrix} \\ g_i(\boldsymbol{x}_J) \end{Bmatrix}. \tag{41}$$

Exchanging the rows to replace the redundant equations by the constraint equation using the procedure outlined in [2] leads to the following equation:

$$\boldsymbol{K} \begin{Bmatrix} \boldsymbol{d}_r \\ \boldsymbol{d}_m \\ \boldsymbol{a} \end{Bmatrix} = \boldsymbol{F} \quad , \tag{42}$$

where $\boldsymbol{K}$ and $\boldsymbol{F}$ are the modified stiffness matrix and force vectors respectively. Knowing $\boldsymbol{a} = \{A_0, B_0, A_1, B_1, \ldots\}^T$ form Equation 42, estimates of the displacement components in radial and axial directions can be obtained using Equations 1 and 2 respectively.

6. Numerical examples

Two static, axisymmetric unbounded problems are presented to illustrate the proposed coupled EFGM-FFEM.

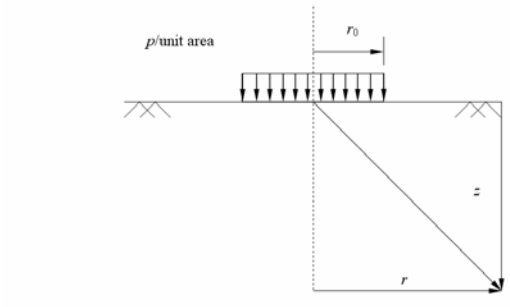

Figure 8. Uniform vertical circular load acting on surface of semi–infinite mass

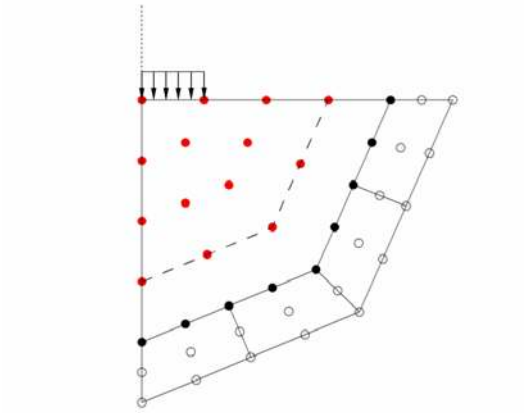

Figure 9. Coupled EFGM–FFEM discretization of semi–infinite mass with uniform vertical circular load acting on surface

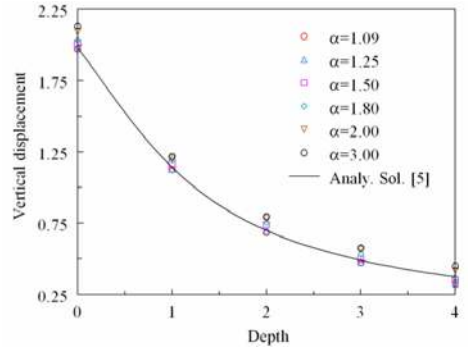

Figure 10. Convergence with similarity ratio (Example 2)

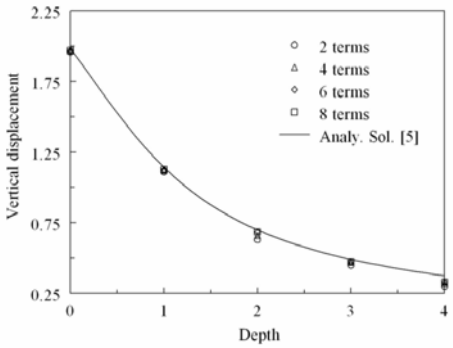

Figure 11. Convergence with number of fractal transformation terms (Example 2)

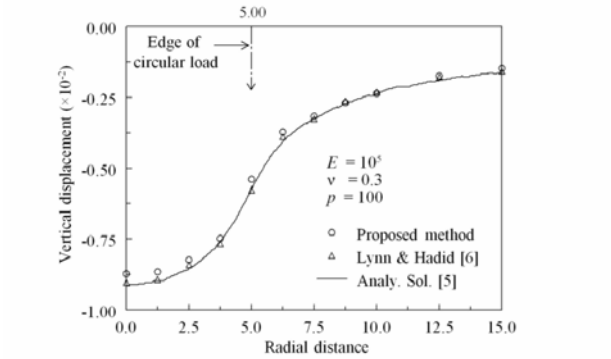

Figure 12. Comparison of radial variation of vertical displacement at $z = 0$ (Example 2)

6.1. Example 1: Uniform Vertical Ring Load Acting on Surface of Semi–Infinite Mass

The deflection of an elastic half-space under a total ring load P with ring load radius r_0, as shown in Figure 3 is considered. The following data were used in the analysis: the material is linearly elastic, with Young's modulus E = 1.0 and Poisson's ratio ν = 0.1, total ring load $P = 1$, and radius of ring load $r_0 = 1.0$. Coupled EFGM-FFEM discretization with L9 fractal mesh configurations having a similarity ratio α of 1.09 are shown in Figure 4. The number of fractal transformation terms used in $\boldsymbol{T}_s^{k-th}$ is 6. Figure 5 shows the convergence of vertical displacement at $r = 0$ with the similarity ratio α employed. Figure 6 shows the convergence of vertical displacement at $r = 0$ with the number of fractal transformation terms used. At the surface $z = 0$, the radial variation of the non-dimensional vertical displacement in terms of $Er_0 / P\left(1-\nu^2\right)$ is shown in Figure 7. The predicted vertical displacement obtained using the proposed method match very well with analytical solution [5] and the solution by Leung *et al*. [4].

6.2. Example 2: Uniform Vertical Load Acting on Surface of Semi–Infinite Mass

Consider the deflection of an elastic half-space under an uniform vertical load p on circular area with radius r_0, as shown in Figure 8. The following data were used in the analysis: the material is linearly elastic, with Young's modulus $E = 10^5$ and Poisson's ratio ν = 0.3, uniform vertical load $p = 100$, and radius of circular area $r_0 = 5$ [38]. Coupled EFGM-FFEM discretization with L9 fractal mesh configurations having a similarity ratio α of 1.09 are shown in Figure 9. Other parameters are same as those used in Example 1. Figure 10 shows the convergence of vertical displacement at $r = 0$ with the similarity ratio α employed. It can be observed from Figure 11 shows the convergence of vertical displacement at $r = 0$ with the number of fractal transformation terms used. At the surface $z = 0$, the radial variation of the vertical displacement is shown in Figure 12. The predicted vertical displacement obtained using the proposed method match very well with analytical solution [5] and the solution by Lynn and Hadid [6].

7. Conclusions

The present study indicates that using the proposed coupled FFEM-EFGM, convergent and accurate solutions can be obtained by adopting an exponential weight function along with the scaling parameter equal to 2.01, 2×2 Gaussian integration in the FFEM region, the number of fractal transformation terms equal to 6, and the similarity ratio closer to unity. The convergence of the solutions with respect to the nodal refinement shows stability. The predicted radial variation of the vertical displacement at the surface $z = 0$, match very well with the analytical solutions.

8. References

1. Belytschko, T., Lu, Y.Y., Gu, L., 1994. Element–free Galerkin methods. International Journal for Numerical Methods in Engineering 37, 229–256.
2. Rao, B.N., Rahman, S., 2000. An efficient meshless method for fracture analysis of cracks. Computational Mechanics 26, 398–408.
3. Leung, A.Y.T., Su, R.K.L., 1995. Mixed mode two–dimensional crack problems by fractal two–level finite element method. Engineering Fracture Mechanics 51(6), 889–895.
4. Leung, A.Y.T., Dai, H., Fok, S.L., Su, R.K.L., 2004. The fractal finite element method for unbounded problems. International Journal for Numerical Methods in Engineering 61, 990–1008.
5. Timoshenko, S.P., Goodier, J.N., 1970. Theory of Elasticity, McGraw–Hill, New York.
6. Lynn, P.P., Hadid, H.A., 1981. Infinite elements with $1/r^n$ type decay. International Journal for Numerical Methods in Engineering 17, 347–355.